Stability of hard plates on soft substrates and application to the design of bioinspired segmented armor

R. Martini, F. Barthelat *

Department of Mechanical Engineering, McGill University, 817 Sherbrooke Street West, Montreal, QC, Canada H3A 2K6

A B S T R A C T

Flexible natural armors from fish, alligators or armadillo are attracting an increasing amount of attention from their unique and attractive combinations of hardness, flexibility and light weight. In particular, the extreme contrast of stiffness between hard plates and surrounding soft tissues give rise to unusual and attractive mechanisms, which now serve as model for the design of bio-inspired armors. Despite a growing interest in bio-inspired flexible protection, there is little guidelines as to the choice of materials, optimum thickness, size, shape and arrangement for the protective plates. In this work, we focus on a failure mode we recently observed on natural and bio-inspired scaled armors: the unstable tilting of individual scales subjected to off-centered point forces. We first present a series of experiments on this system, followed by a model based on contact mechanics and friction. We condense the result into a single stability diagram which capture the key parameters that govern the onset of plate tilting from a localized force. We found that the stability of individual plates is governed by the location of the point force on the plate, by the friction at the surface of the plate, by the size of the plate and by the stiffness of the substrate. We finally discuss how some of these parameters can be optimized at the design stage to produce bio-inspired protective systems with desired combination of surface hardness, stability and flexural compliance.

© 2016 Elsevier Ltd. All rights reserved.

1. Introduction

Over millions of years, evolutionary pressures have led to high-performance protecting materials and systems, emerging from an "arm's race" between predators and preys. These natural armors, which include mollusk shells, testudines carapace and arthropods exoskeleton, display a wide range of compositions, architectures and sizes to resist a variety of threats such as sharp puncture, laceration or crushing. The armor of animals with fast locomotion presents particularly interesting features. These protective materials must be hard to resist puncture, yet compliant and light to allow for unimpeded movement. In natural organisms this design contradiction is often resolved by segmentation of the hard protective layer into plates of finite size. Typical examples of segmented armors include the scaled skins of fishes and snakes or the osteoderms of armadillos and crocodiles. These natural dermal armors are light-weight, locally hard to resist puncture and yet flexible at larger length scales to allow for motion (Vernerey and Barthelat, 2010).

Manmade segmented armors were already used in ancient times, for example in Roman antiquity (Hamblin, 1996) or
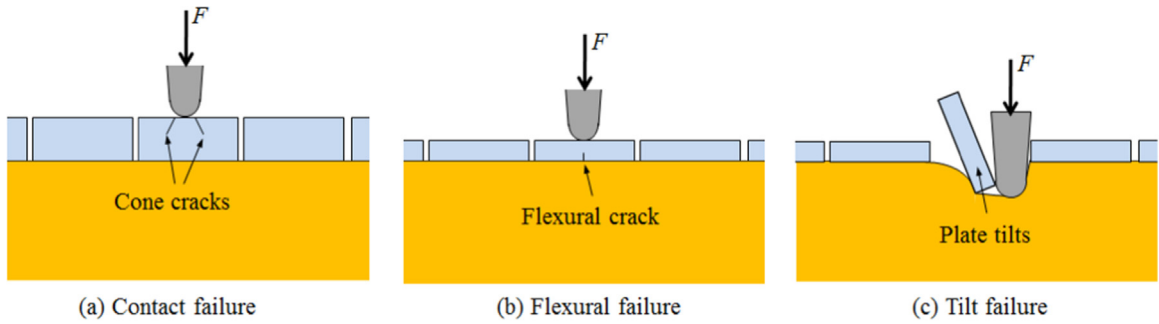

Fig. 1. Three possible failure modes for segmented stiff plates on soft substrate subjected to indentation.

Japanese medieval times (Robinson, 2002). More recently, a protective equipment based on individual ceramic plates was patented under the name of "Dragon Skin" (Neal, 2003). Modern applications include personal armor systems, industrial protective gear or compliant robotics. Despite a growing interest in bio-inspired flexible protection, there is little guideline for the choice of materials, optimum thickness, size, shape and arrangement for the protective plates. Flexible natural armors can provide a powerful source of inspiration to design and optimize better synthetic protective systems. In recent years, the performance and mechanics of armadillo's carapace (Chen et al., 2011) and fish skin (Zhu et al., 2012; Yang et al., 2013a, 2013b, 2014) was systematically studied. These studies mainly focused on the mechanical response of individual scales subjected to indentation and/or uniaxial tension (Bruet et al., 2008; Zhu et al., 2012; Yang et al., 2014; Lin et al., 2011; Marino Cugno Garrano et al., 2012). Scale-substrate and scale-scale interactions play an important role in resisting predator
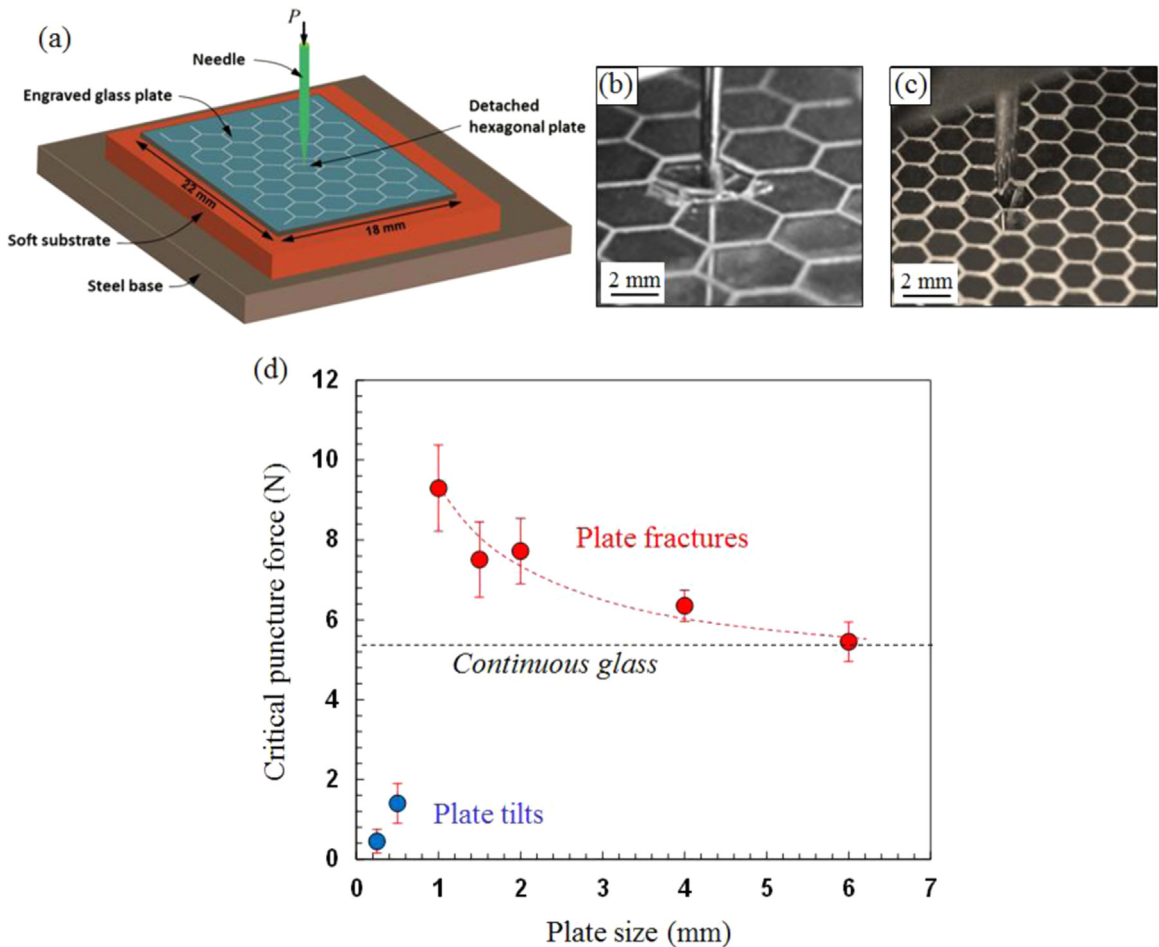

Fig. 2. Puncture experiments on segment glass layer on a soft substrate: (a) experimental setup; in-situ images showing (b) flexural failure and (c) tilt failure; (d) critical puncture force as function of plate size: the critical puncture force increases when the plate size is reduced, but below a critical threshold (plate size ~0.75 mm) the critical force is much lower because the plate tilts (adapted from Chintapalli et al., 2014).

attacks (Vernerey and Barthelat, 2010). These insights have inspired new flexible protective systems which combine compliance and surface hardness (Chintapalli et al., 2014; Rudykh et al., 2015; Ghosh et al., 2014; Funk et al., 2015). A common characteristic to all natural protective systems is the extreme contrast of stiffness between the protective material and the soft underlying tissues. For example, the elastic modulus of teleost fish scales is five orders of magnitude higher than the modulus of the underlying skin (stratum compactum) and of the soft underlying tissues (muscles, other organs) (Zhu et al., 2012). In terms of mechanics, large contrasts of stiffness between a thin film and its substrate lead to a rich set of failure modes. Fig. 1 shows three possible failure modes for segmented stiff plates on soft substrate subjected to sharp puncture (i.e. the radius of the indenter is significantly smaller than the dimensions of the plates).

Depending on the relative stiffness of the film and substrate and the thickness of the film, spherical indentation on a stiff film may lead to conical cracks initiated by contact stresses (Fig. 1(a)), or to radial cracks initiated by flexural stresses (Fig. 1(b)) (Lawn et al., 2002). The transition between these two failure modes is important for a variety of applications, and it can be captured using relatively simple models (Lawn et al., 2002). Chintapalli et al. (2014) recently demonstrated that for high contrast of stiffness between plates and substrate and for the case where the failure of the plates is governed by flexural stresses, segmented plates increase the resistance to puncture compared to continuous coatings (Fig. 2). Segmenting the hard layer therefore not only makes the system more compliant in flexion, it also increases the resistance to sharp puncture. Other recent studies (Zhu et al., 2013; Browning et al., 2013) demonstrated that the interaction between neighboring scales redistributes puncture stresses over large areas, delaying blunt damage and preventing injury of the soft underlying tissues.

Recent experiments of sharp puncture on segmented plates highlighted a third failure mode (Chintapalli et al., 2014) where the indented plate suddenly tilts, resulting in the fast sliding of the indenter onto its surface and into the substrate (Figs. 1(c) and 2(c)). While this failure mode does not damage the plate, it is highly detrimental because the rapid tilting of the plate exposes the soft and fragile substrate to the tip of the indenter.

Interestingly, we also observed this failure mode in puncture tests on gar fish skin. Gar are heavily armored fish with thick and bony ganoid scales with outstanding hardness and toughness (Yang et al., 2013a). When the skin of gar fish is punctured with a sharp needle, individual scales to not fracture (even when the needle is pressed in the center of a scale). Instead, at a critical puncture force the indented scale suddenly tilts, the needle rapidly slides on its surface and reaches easy access to the soft underlying tissue between the scales (Fig. 3). The tilt of the plate is sudden and unstable, and leads to a sharp drop of puncture force (Fig. 3(a)). Our repeated attempts to fracture individual gar scales by puncture were not successful, and the scale invariably tilted instead of fracturing. Evidently, in this case the resistance of the scaled skin to sharp puncture is not governed by the strength of the individual scales, but rather by their ability to resist tilting.

These observations have important implications in terms of design: a segmented armor, even if made of extremely strong materials, could be easily defeated by simple tilting of the plates. To the best of our knowledge, the stability of hard plates on
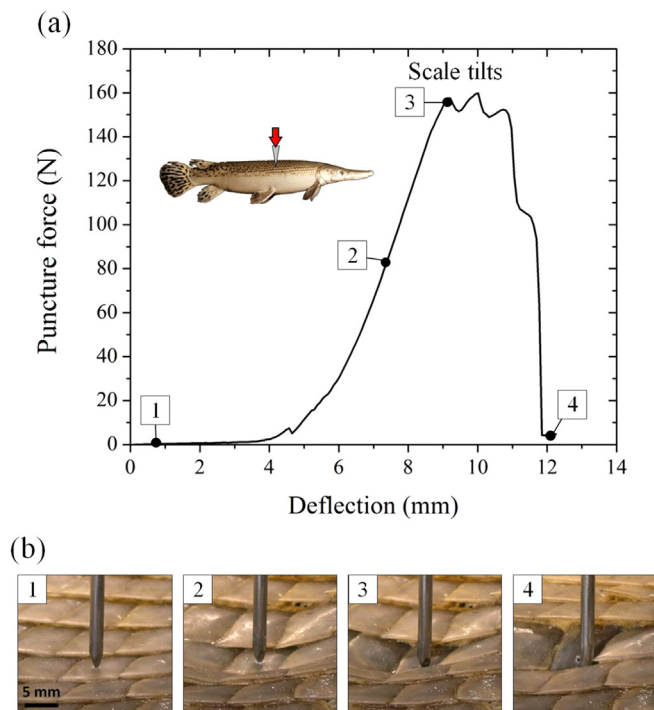

Fig. 3. Puncture test of gar fish skin on a soft substrate. (a) Typical force–deflection curve and (b) sequence of images acquired during the test. At a critical force the indented scale suddenly tilts, and the needle rapidly reaches the underlying soft tissues. This instability is accompanied by a sharp drop of the puncture force.
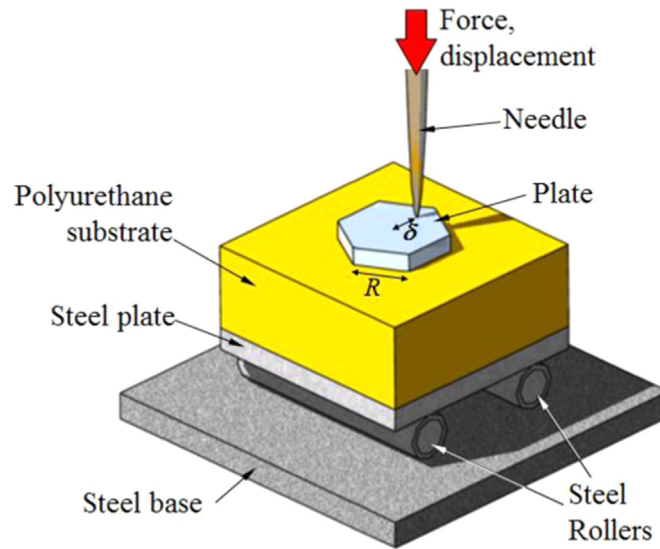
Fig. 4. Experimental setup for the puncture tests.

soft substrates and the tilt failure have not been studied in the past, and the objective of the present work is to investigate this dangerous failure mode. We first present a series of puncture experiments performed on individual glass plates on soft substrate using different parameters (position of the indent on the plate, friction coefficient between needle and plate). A model is then proposed to predict the force at which the plate becomes unstable and tilts, and to identify the parameters that govern the stability of the plate. These findings provide new guidelines for delaying this dangerous failure mode in bio-inspired segmented armor. The results may also be relevant to other problems such as the stability of buildings on soft foundations or the design of probes to measure soft materials underneath layers with hard inclusions.

2. Experimental setup

Following our previous work on bioinspired flexible armor (Chintapalli et al., 2014), the experiments consisted of indenting hexagonal glass plates resting on a soft elastomeric substrate. The hexagonal shape was chosen because hexagon tiles can continuously tessellate the surface of the soft substrate, and because it is similar to the shape of natural scales and osteoderms (Vickaryous and Hall, 2006). Hexagonal plates (size $R=5$ mm for the entire study) were cut with a three dimensional laser engraver (Vitro Laser Solutions UG, Minded, Germany) from a 1 mm thick borosilicate glass (Young's modulus=63 GPa (Mirkhalaf et al., 2014)). The hexagons were then either placed or glued on a 13 mm thick polyurethane substrate (Fig. 4). Puncture tests were performed with steel needles of two different geometries: a "sharp" needle with a tip radius of 70 μm, and a "blunt" needle with a tip radius of 130 μm. The position of the tip of the needle on the plate was defined by the offset distance δ from the center of the hexagon, which was varied for different experiments. The position of the needle tip onto the plate could be adjusted to ± 250 μm. However once the needle was in place, the optical measurement of the offset distance was more accurate (error of ± 125 μm). The tilting of the plate involved forces and displacements in the plane of the plate. In order to simplify the interpretation of the experiments, the substrate–plate assembly was placed on two rollers whose axis was perpendicular to the direction of the offset (Fig. 4). The rollers ensured that the base did not constrain horizontal motions, with the implication that the needle only carried axial forces. The soft substrate was preconditioned before every experiment in order to avoid hysteresis in mechanical response from the Mullins effect, and its stiffness was measured by indentation with a spherical indenter following the method described by Zhu et al. (2012). A shear modulus of $\mu_S=50$ kPa was determined for the substrate, corresponding to a modulus $E_S=150$ kPa (using Poisson's ratio $\nu_S=0.5$ consistent with the incompressibility of the elastomeric substrate).

The puncture tests were performed using two configurations: a "non-bonded" configuration where the plate simply rested on the soft substrate, and a "bonded" configuration where the plate was glued to the substrate using cyanoacrylate. For the bonded cases, the adhesion was sufficiently strong to keep the plate bonded on the substrate even in the post-instability stages. The puncture tests were performed with a miniaturized loading stage (Ernest Fullam, NY) at a constant velocity of 20 μm/s. Displacements were recorded with a LVDT, and the force were recorded using a 45 N capacity load cell. In addition, pictures of the sample were acquired with an digital camera (Olympus Camedia C-5060) in micro-focus mode before the test commenced in order to measure the offset distance accurately, and then at regular intervals during the test to monitor the tilt angle of the plate.
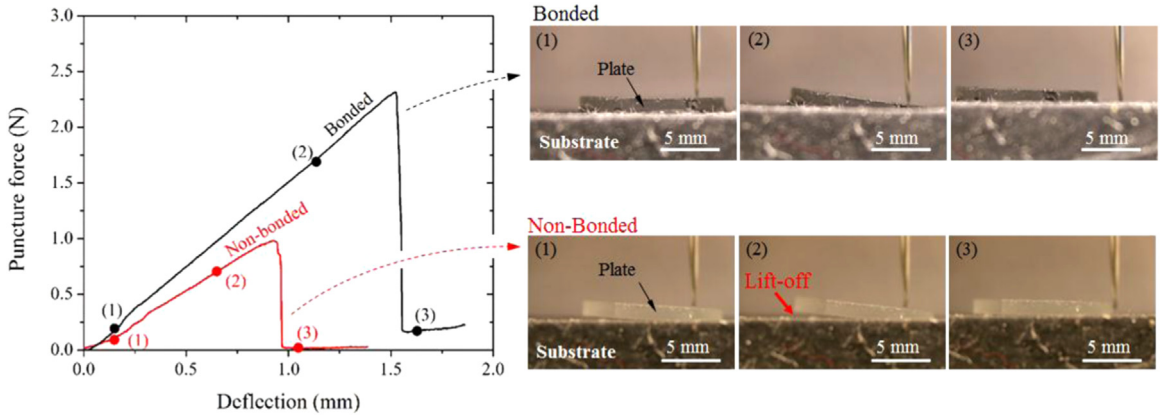
Fig. 5. Typical puncture force–deflection curves for the cases of bonded and non-bonded plates. The red arrow shows that the edge of the plate lifts-off for the non-bonded case with large offset distance. (For interpretation of the references to color in this figure legend, the reader is referred to the web version of this article.)
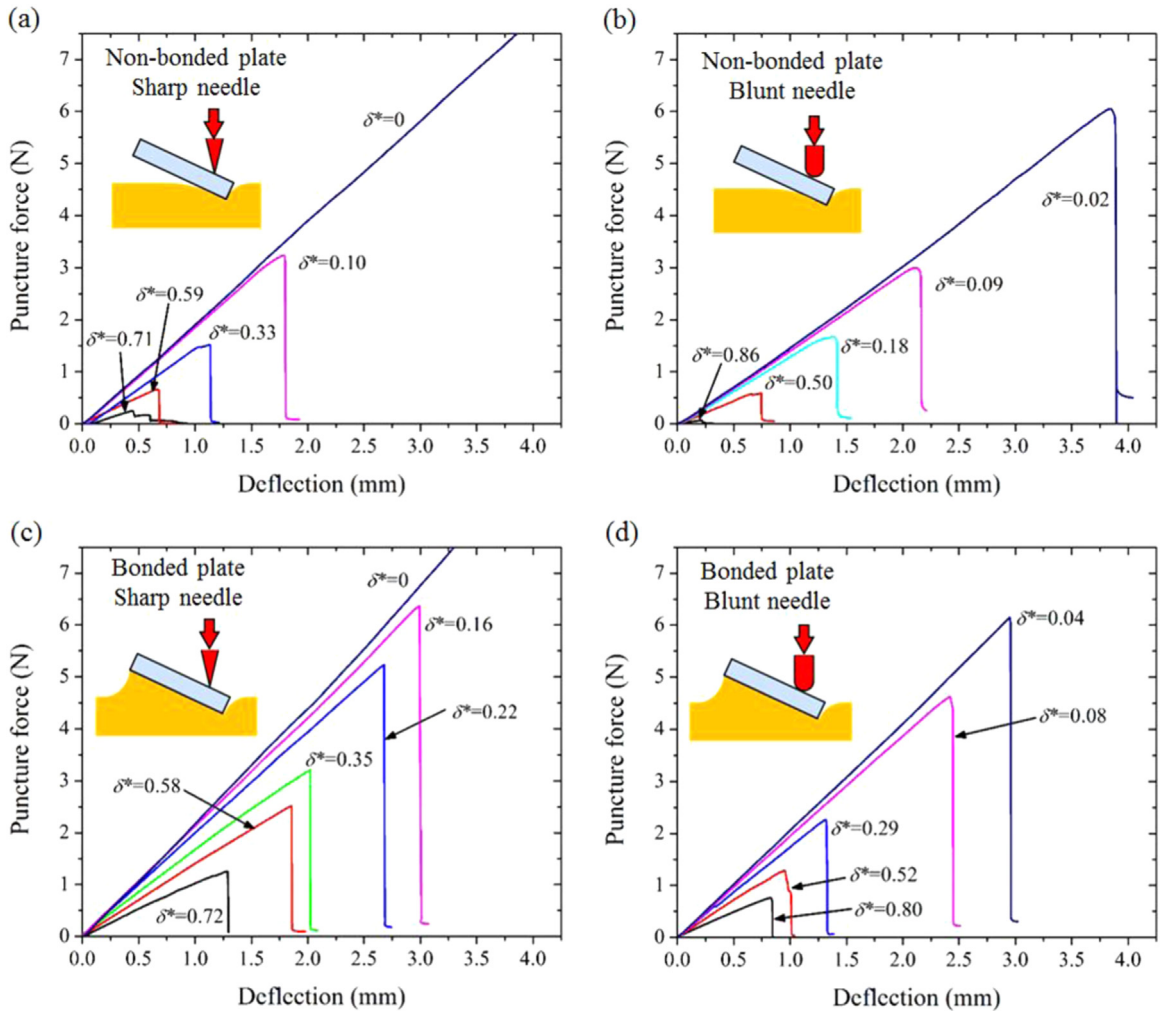

Fig. 6. Force–deflection curves for difference combination of bonded/nonbonded plate and sharp/blunt needle. For each case, the results of tests with different normalized offset distance $\delta^* = \delta/R$ are shown.
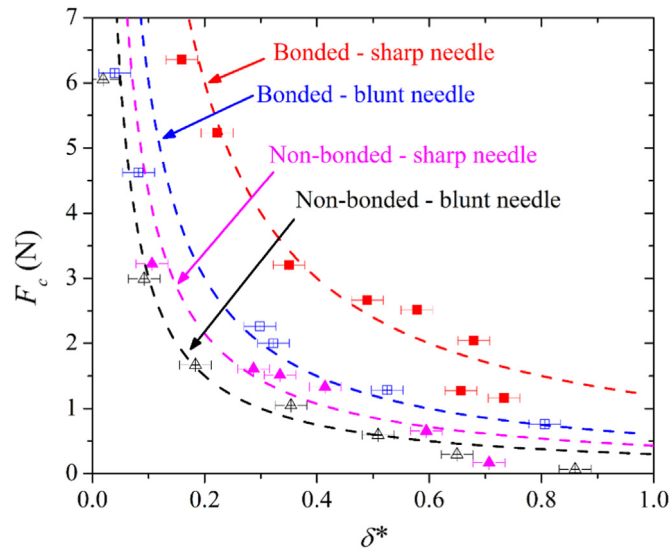
Fig. 7. Critical force F_c as function of the non-dimensional offset for the bonded plate configuration (square) and non-bonded plate configuration (triangles) in the case of puncturing with sharp (empty symbols) and blunt (full symbols) needle. The dash lines represent fitting curves of the form $F_c = \alpha/\delta^*$, where α is a fitting parameter. The bars represent the errors on the measurement of the offset distances and on the force (the errors on the forces are too small so see on the graph).

3. Results

Fig. 5 shows two typical puncture force–displacement curves for the cases of non-bonded and bonded plate, together with a sequence of pictures taken during the experiments (for the two cases shown in Fig. 5, the offset was $\delta = 3.75$ mm).

In the first stage of the experiment, the needle progressively pushed the plate into the soft substrate, with a linear response on the force–deflection curve (stage (1) in Fig. 5). As the displacement increased the puncture force–displacement response remained linear, but the plate progressively tilted (stage (2) in Fig. 5). The puncture stiffness was lower for the non-bonded case, because of partial lift-off of the plate from the substrate (indicated by a red arrow in Fig. 5). Despite the tilt of the plate, the tip of the needle remained at the same position during stage (2) because of frictional forces. At a critical puncture force F_c, the tip of the needle suddenly slid on the surface of the plate, the plate rapidly tilted and the needle punctured the substrate. This onset of instability translated into a sharp drop in the puncture force (stage (3) in Fig. 5). Fig. 6
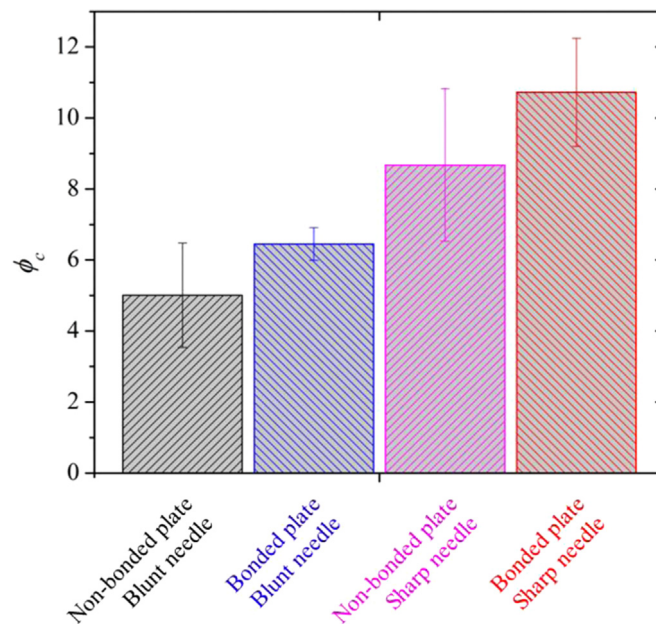

Fig. 8. Critical tilt angle measured during the experiments for the four configurations. Higher critical angles are reported for the experiments with the sharp needle. The critical angle is univocally associated to a value for the friction coefficient.

shows a more complete series of typical force–deflection curves obtained from puncture tests of non-bonded and bonded plates, using sharp and blunt needles (i.e. four different combinations corresponding to Fig. 6(a)–(d)).

Within each of these four configurations, puncture tests were performed at different normalized initial offset distances $\delta^* = \delta/R$. All the curves showed the same behavior described above, with a quasi-linear increase in force–deflection followed by a sharp drop in force. In all configurations both puncture stiffness and critical puncture force decreased for higher δ^*, the effect being more pronounced for the bonded plate case. For the cases $\delta^* = 0$ the puncture force increased to much higher values than for the cases $\delta^* > 0$, and these tests were interrupted before the plate fractured. Fig. 7 shows the critical puncture force F_c as function of δ^*. The series of individual tests at various locations on the tablets all followed the same trend, and for all configurations F_c appears to be roughly inversely proportional to δ^*. The results also show that the plate is more stable (i.e. higher F_c) when it is bonded to the substrate, and when a sharper needle is used.

The critical angle at the onset of instability ϕ_c was also measured using the images acquired in-situ, and the results are shown in Fig. 8. The critical angle is higher for the experiments performed with the sharp needle ($\phi_c \sim 9°$ and $\phi_c \sim 10°$ for the non-bonded and bonded plate configurations, respectively) compared to experiments performed with the bunt needle ($\phi_c \sim 5°$ and $\phi_c \sim 6°$ for the non-bonded and bonded plate configurations, respectively).

The experiments with the sharp needle left scratches on the surface of the glass plate, which indicated a plowing mechanism that can increase the coefficient of friction between the needle and the surface of the glass plate (Blau, 2001). The bonded configurations appeared to produce a higher critical angle, although the difference was small (one degree) and in the order of the accuracy of the measurement for the tilt angle. The critical angles for the blunt and sharp needles were $\phi_c = 5.73° \pm 1.28°$ and $\phi_c = 10.21° \pm 1.78°$ respectively.

4. Model

In this section we present a model that captures the parameters governing the onset of stability of a stiff plate on a soft substrate. Natural scales and bony plates in osteoderms are typically several orders of magnitude stiffer than the underlying soft tissue they protect. Likewise, in our experiments the glass plates were six orders of magnitude stiffer than the underlying elastomeric substrate. More generally, surface hardness is required for the plates to resist penetration from sharp indenters. Since hard materials are usually stiff (Ashby, 2005), the assumption of very stiff plates is a reasonable starting point for the modeling and design of scaled armor made of homogeneous plates. We therefore modeled the plates as rigid plates, the deformations in the system being entirely absorbed by the softer substrate. In addition, we assumed a circular shape for the plates in order to simplify calculations. The substrate was modeled as a semi-infinite block of linear elastic material.

4.1. Free body diagram

Fig. 9 shows a cross-section of a rigid circular plate on a soft substrate. The action of the needle onto the plate is modeled by a point force F applied onto the plate at an offset distance δ from the center of the plate. Under the effect of this force, the plate simultaneously sinks into the soft substrate and tilts (if $\delta > 0$). To capture this kinematics we defined the displacement u_0 along the z axis of the center of mass for the plate, and the tilt angle ϕ of the plate about the y axis (Fig. 9b). The applied force F is vertical (i.e. along axis z) because in the experiments the rollers placed under the substrate prevent any horizontal force form being transmitted through the system. F can be decomposed in a normal component $N = F \cos \phi$ and a tangential component $T = F \sin \phi$, T corresponding to the static frictional force between the needle and the plate. Under the effect of F the plate deforms the substrate, which generates a reaction force in the form of a distributed pressure $p(x,y)$ (Fig. 9b).

As the puncture force F increases the tilt angle ϕ increases, which results in an increase of the tangential force T. Following simple Coulomb friction, the tip of the needle will remain at the same position on the plate as long as $T < fN$
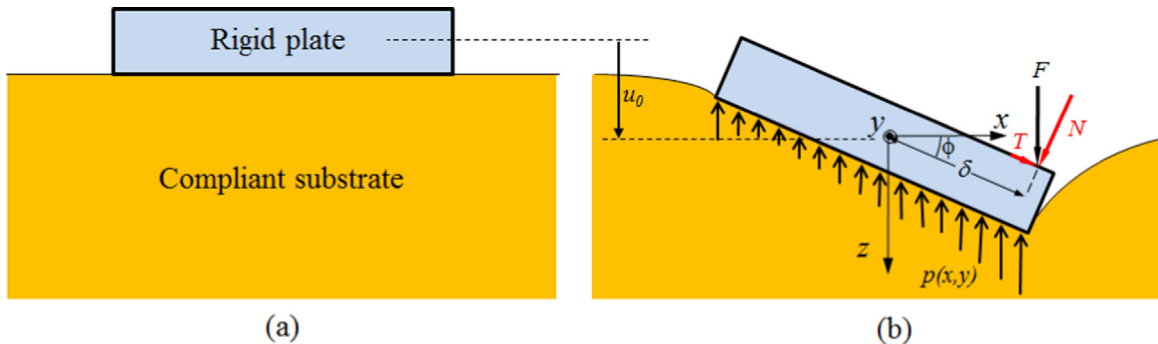

Fig. 9. (a) Initial configuration: rigid plate of finite size resting on a soft substrate; and (b) free-body diagram of the plate subjected to a puncture at an offset distance δ from the center of the plate.

where f is the static coefficient of friction between the needle and the plate. When the tangential force T reaches the Coulomb frictional force, the tip of the needle starts sliding on the plate. By equating the tangential force and the Coulomb frictional force, the critical angle ϕ_c at the onset of sliding can be computed using $fF_c \cos \phi_c = F_c \sin \phi_c$. This provides a simple relation between the critical angle and the friction coefficient between the needle and the plate

$$\tan \phi_c = f \tag{1}$$

Once the critical tilt angle is reached, the sliding of the needle results in a new configuration of applied forces which cannot be sustained by static equilibrium. The sliding of the needle rapidly tilts the plate in an unstable fashion until the needle reaches the edge of the plate and penetrates the soft substrate. In the experimental force–deflection curves, this rapid event corresponded to a sudden decrease in puncture force. The friction coefficient can be determined with Eq. (1) from the critical tilt angle measured experimentally. This simple procedure yielded a friction coefficient $f \sim 0.1$ for the blunt needle, and $f \sim 0.18$ for the sharp needle. The higher coefficient of friction for the sharp needle can be explained by plowing mechanisms (Blau, 2001) suggested by the scratches on the surface of the plates when a sharp needle was used.

4.2. Contact mechanics

In this section we develop the model further with the objective to capture the effects of plate size, offset distance, substrate stiffness and friction coefficient on the onset of instability for the plate. The model requires the details of the pressure distribution $p(x,y)$ over the contact area between the plate and the substrate (Fig. 9b). Since the stiffness of the plate is several orders of magnitudes stiffer than the substrate, we modeled the plate as a rigid punch pressing onto a deformable substrate. We used a closed-form solution for the indentation of elastic half-spaces with a punch of general shape, which was first developed by Sneddon (1965) in terms of Hankel transforms, and then extended to punches of arbitrary shape by Fabrikant (1986). In this solution a frictionless contact was assumed, and the punch was assumed to be in complete and continuous contact with the substrate. Following this solution, an imposed displacement u and a tilt angle ϕ on a circular punch of radius R generate a force F and a moment M following (Fabrikant, 1988):

$$\begin{cases} F = \dfrac{4\mu R}{1-\nu} u \\ M = F\delta = \dfrac{8}{3} \dfrac{\mu R^3}{1-\nu} \phi \end{cases} \tag{2}$$

where μ and ν are the shear modulus and Poisson's ratio for the substrate, respectively. This solution was used for the cases where the plates remain in full contact with the substrate, which is the case for small offset distances ($\delta/R < 1/3$) (Barber, 1984). For larger offset distances, the plate partially loses contact with the substrate and a close-form solution is not available. In the case of partial lift-off, a semi-analytical solution can be obtained by numerically integrating the Boussinesq solution over the surface of an elastic half-space

$$u_z(x, y) = \frac{1-\nu}{2\pi\mu} \iint_{A_c} \frac{p(\xi, \eta)}{\sqrt{(x - \xi)^2 + (y - \eta)^2}} d\xi d\eta \tag{3}$$

where $u_z(x, y)$ is the displacement of the surface of the half space imposed by the pressure distribution $p(\xi, \eta)$, and A_c in the contact area between the plate and the substrate. Using the symmetry of the system about the yz plane, only half of the plate was modeled. The solution of Eq. (3) must fulfill two conditions: (i) the plate and the elastic half-space cannot interpenetrate in the area of the plate that is not in contact with the substrate (A_l) and (ii) the contact pressure between the plate and the substrate in the contact area (A_c) must be positive everywhere. These conditions can be written as

$$u_z(x, y) > u_0 + \phi x \quad \text{in} \quad A_l$$
$$p(\xi, \eta) > 0 \quad \text{in} \quad A_c \tag{4}$$

where u_0 is the vertical displacement of the center of the plate and ϕ is the tilt angle about the y axis. We use the normalized coordinates $x^* = \frac{x}{R}, y^* = \frac{y}{R}, \xi^* = \frac{\xi}{R}, \eta^* = \frac{\eta}{R}$, the normalized displacements $u_z^*(x^*, y^*) = u_z(x^*, y^*)/R, u_0^* = u_0/R$, normalized pressure $p^*(\xi^*, \eta^*) = \frac{1-\nu}{2\pi\mu} p(\xi^*, \eta^*)$ and normalized contact area $A_c^* = A_c/\pi R^2$. Using this non-dimensional formulation and substituting the surface displacements imposed by the plate, Eq. (3) can be rewritten as

$$u_0^* + \phi x^* = \iint_{A_c^*} \frac{p^*(\xi^*, \eta^*)}{\sqrt{(x^* - \xi^*)^2 + (y^* - \eta^*)^2}} d\xi^* d\eta^* \tag{5}$$

To solve this equation, the penetration and tilt angle were set to a fixed value. The pressure distribution at the interface was then computed by meshing the indented area into different sectors, and by assuming a constant contact pressure within each of these sectors. With this approach, the integral Eq. (5) transformed into the linear system
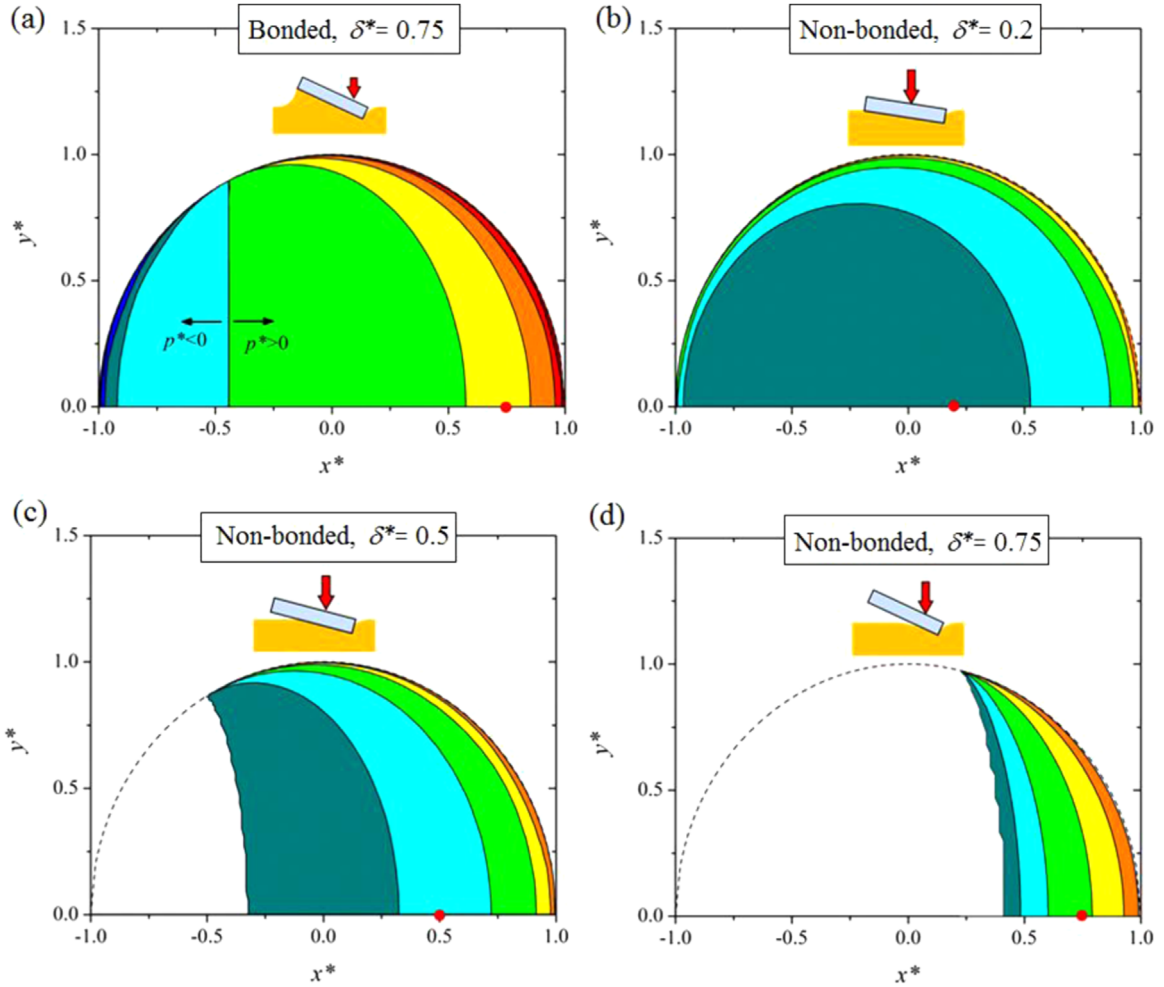
$$u_i^* = K_{ij} p_j^* \tag{6}$$

Fig. 10. Half contact areas and distribution of pressure $p^*(x^*,y^*)$ for the cases of (a) bonded plate, $\delta^*=0.75$ (exact solution); non-bonded plate (numerical solutions) with (b) $\delta^*=0.2$, (c) $\delta^*=0.50$ and (d) $\delta^*=0.75$. The high-gradients of pressure near the edge of the plate indicate a stress singularity. For all cases, the red dot shows the application point of the force F^*. (For interpretation of the references to color in this figure legend, the reader is referred to the web version of this article.)

where K_{ij} is the influence matrix linking the normalized displacement in the element i to the normalized contact traction in the element j. Eq. (6) was solved numerically using an initial guess for the contact area. From the second iteration, the contact was partially released to fulfill the constraint of a positive pressure in the contact area. The meshing of the plate area was made finer along the edge of the plate in order to accurately capture the pressure singularity. In a typical model less than five iterations were needed to ensure a converged configuration where the contact area did not change. Once $p^*(x^*, y^*)$ was computed numerically, the magnitude of the non-dimensional force $F^*=\frac{1-\nu}{2\pi\mu R^2}F$ was computed by simply integrating $p^*(x^*, y^*)$ over the contact area A_c^*. The application point of this force was finally determined by numerically computing the center of pressure of $p(x, y)$, providing the offset distance δ^* corresponding to that particular tilt angle. Once this computational scheme was in place, we systematically explored the relationships between the vertical displacement u_0^*, the tilt angle of the plate ϕ, the normalized puncture force F^* and the normalized offset distance δ^*. Fig. 10 shows four examples of pressure distributions obtained from these models. For the case where the plate is bonded (Fig. 10(a)), the closed-form solution (Fabrikant, 1988) was used. This solution predicts that for large offset δ^* ($\delta^*=0.75$ is shown in Fig. 10(a)), the tilt is significant and the pressure distribution shows a tensile region (i.e. $p^* < 0$). In the non-bonded cases the interface can only sustain positive pressures, and our numerical scheme was used to compute the solution. The case $\delta^*=0.2$ (Fig. 10(b)) shows full contact because $\delta^* < 1/3$, and we recovered the close form solution (Fabrikant, 1988). The cases $\delta^*=0.50$ and $\delta^*=0.75$ (Fig. 10(c) and (d)) show partial lift-off of the plate and a reduced contact area, this effect being more pronounced for larger δ^*. Bonding of the plate and/or small offset distances favor the redistribution of the pressure over a larger area, which reduces the strains in the substrates. For an animal with hard segmented plates, this would mean a lower risk of blunt injuries from the tilting of the hard plates. An interesting feature of the solution is that once δ^* is fixed, the deflection u_0^*, the force F^* and the tilt angle ϕ increase during the test, but the contact area A_c^* remains constant even with lift-off. Because
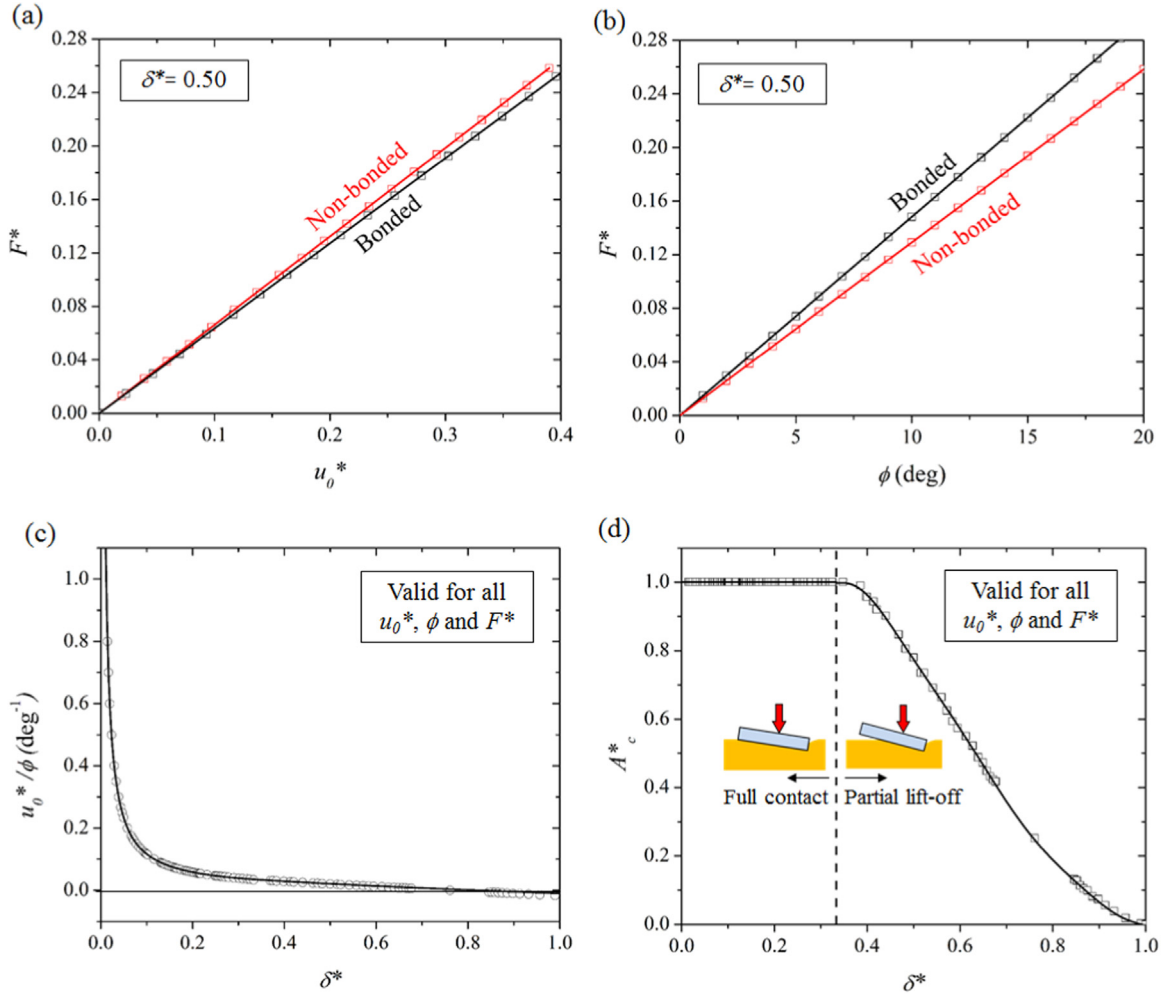
Fig. 11. Results of the models for the bonded and non-bonded cases: (a) force F^* as function of the displacement of the center of mass of the plate u_0^*, for the case $\delta^*=0.50$; (b) force F^* as function of tilt angle for non-bonded and bonded plates, for $\delta^*=0.50$ (c) ratio u_0^*/ϕ and (d) contact area A_c^* as a function of the normalized offset δ^* for the un-bonded plate. The results (c) and (d) are independent from u_0^*, ϕ and F^*. The markers corresponds to points where the simulations were performed.

the contact area does not change once δ^* is fixed, the force F^* increases linearly with u_0^* until the instability point is reached (Fig. 11(a)), which is consistent with our experimental observations (Figs. 5 and 6).

For the purpose of capturing the onset of instability in this system, we also examined how the tilt angle ϕ increased. Fig. 11b shows F^* as function of ϕ for an offset $\delta^*=0.50$, and for the cases of bonded and non-bonded plates. As expected, the tilt angle increases more rapidly with F^* when the plate is not bonded to the substrate. This plot illustrates another general feature of the model: whether the plate is bonded or non-bonded with or without partial lift-off, the tilt angle ϕ increase linearly with the force F^*. Since the displacement u_0^* and the force F^* are also related in a linear fashion, the ratio u_0^*/ϕ does not depend on F^* and is function of δ^* only. This ratio between the displacement and the tilting of the plate characterizes how the plate reacts to an off-centered force. Fig. 11c, shown for the case of a non-bonded plate, shows that u_0^*/ϕ is strongly dependent on δ^*. Applying a point force near the center of the plate (i.e. small δ^*) mostly results in the plate sinking into the substrate, with little tilt (i.e. high u_0^*/ϕ). For slightly higher δ^* (greater than 0.05–0.1), tilting of the plate dominates over displacement into the substrate (i.e. low u_0^*/ϕ). For $\delta^* > 0.77$, the tilt is so pronounced that the center of mass of the plate moves upwards and away from the substrate (u_0^*/ϕ is negative). Fig. 11b shows the contact area A_c^* as function of δ^*. For $\delta^* < 1/3$ the plate remains in full contact with the substrate ($A_c^*=1$), which is consistent with previous models (Barber, 1984). For $\delta^* > 1/3$, lift-off occurs and the contact area decreases almost linearly with δ^*, down to $A_c^*=0$ for $\delta^*=1$.

The solutions developed above can now be used to predict the onset of tilt instability for the plate. The critical tilt angle ϕ_c at which the needle will slide on the plate is given by $\tan \phi_c=f$ where f is the coefficient of friction between the needle and the plate. The critical puncture force F_c^* at the onset instability was then determined from ϕ_c using the model developed above. This calculation can be repeated for any combination of offset distance δ^* and coefficient of friction f, and the results are summarized in a "stability diagram" shown in Fig. 12.
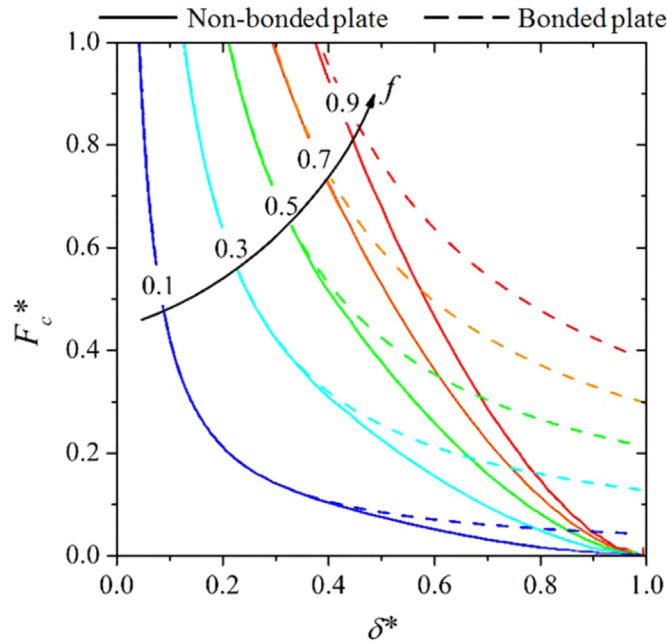
Fig. 12. Stability diagram for a non-bonded plate a bonded plate: for each case the critical puncture force F_c^* is given as function of the offset distance δ^* and the friction coefficient f.

The diagram predicts a rapid decrease in critical puncture force F_c^* as the offset distance δ^* is increased. The diagram also clearly shows how the stability of the plate increases when the friction coefficient f is increased. More specifically, for any given offset distance δ^*, the critical puncture force F_c^* increases linearly with friction coefficient. The critical force for bonded and non-bonded plate configurations are identical for $\delta^* < 1/3$ which is expected, since in that case the non-bonded plate remains in full contact with the substrate. However for larger offsets $\delta^* > 1/3$ the two models diverge, the non-bonded case displaying lower critical puncture force F_c^*. As expected, for large offset distances the bonded plate is more stable that the non-bonded plates (i.e. the critical force is higher). As δ^* approaches $\delta^*=1$ the non-bonded plate configuration does not provide any resistance to tilting and F_c^* approaches zero. In contrast, the bonded plate can still display a stable behavior even for $\delta^*=1$. This diagram therefore presents a condensed snapshot of the mechanics of the plate, and of conditions for stability which can be used in the design of bio-inspired flexible armor.
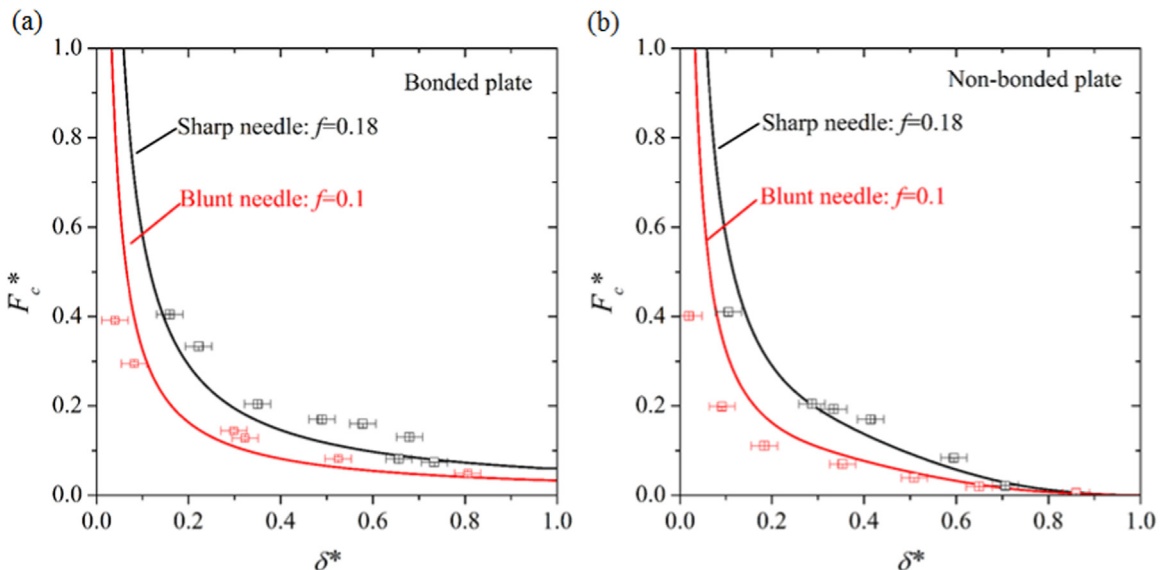

Fig. 13. Comparison between the model and the experimental results for (a) non-bonded and (b) bonded configurations. In both graphs, the red lines and squares represent the results obtained with the blunt needle while the black lines were obtained with the sharp needle. (For interpretation of the references to color in this figure legend, the reader is referred to the web version of this article.)

Before the diagram is discussed in the context of design, we compare the stability onsets predicted by the model with the experimental results reported in the previous section. The parameters of the model were obtained experimentally and independently, and no curve fitting was used to match the model with the experiments. Since we used hexagonal plates in the experiments, we made small modifications to the models to implement the hexagonal geometry of the plates. The friction coefficients for sharp and blunt plate were determined from the critical tilt angle as described above. Fig. 13(a) and (b) shows that whether the plate is bonded or non-bonded, our model agrees well with the experimental results, validating our model for the predictions for the onset of stability for individual plates.

5. Strategies to improve stability

The model developed here suggests four strategies to enhance the overall stability of the protective plates: (i) bonding the plates onto the substrate; (ii) increasing the coefficient of friction; (iii) increasing the size of the plate and (iv) increasing the stiffness of the substrate. These four design parameters are discussed in more details below.

(i) *Bonding*: Our experiment and model show how bonding the plate to the substrate increases their stability. Similar stabilizing effects can be achieved, more generally, by constraining the tilting of the plates by increasing the interaction of plates with their neighbors. These interactions can be achieved by ligaments between the plates (e.g. Sharpeys' fibers that connect armadillos osteoderms), interlocking patterns (e.g. sutures between turtles scutes), direct mechanical interactions between scales (scaled skin of snakes) or scale engagement through direct contact for certain curvature of the skin (scaled skin of garfish).

(ii) *Friction*: The second approach to enhance stability consists in increasing the friction coefficient between the indenter and the plate by, for example, increasing surface roughness. We explored this strategy experimentally by coating the glass plates with a thin layer of cyanoacrylate and, in another case, with a layer of sandpaper (grit #60). The specimens with the modified surface roughness were tested by following the same experimental protocol to measure the friction coefficient and the critical force for tilting instability, using the sharp needle. Fig. 14 displays the normalized critical force as function of the offset distance and for different friction coefficients. The experimental data are again compared with the analytical model (dash line) for further validation of the model, where the friction coefficients were evaluated from the critical tilt angle (0.23 for the cyanoacrylate layer and 0.67 for the sandpaper). Compared to the bare glass surface, the cyanoacrylate and sandpaper surfaces increases the critical force or all offset distances. The sandpaper, which provides the highest coefficient of friction amongst the tested sample, induces a six-fold improvement of the critical force for tilt instability over the bare glass surface.

Since the stability of the plate can be increased by increasing the resistance of the needle to sliding, a related approach would consist in designing surface morphologies that "trap" the tip of the needle at pre-defined positions on the plate. In nature these morphologies may include the concentric patterns of regions with different roughness, such as in teleost scales (Zhu et al., 2011). The osteoderms in the pelvic and pectoral shields of armadillo's dermal armor also display trenches (Chen et al., 2011) (Fig. 15(a)) which may prevent the predator's teeth from reaching the weak interfaces between the osteoderms.
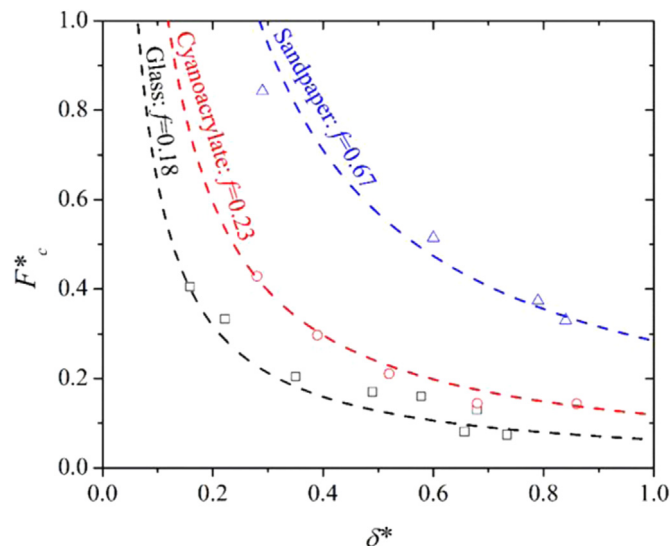

Fig. 14. Comparison of the critical force F_c^* for bonded rigid plates with different top surfaces: bare glass, thin cyanoacrylate layer and sandpaper. The symbols represent the experimental results and the dashed lines show the stability onset as predicted by the model.
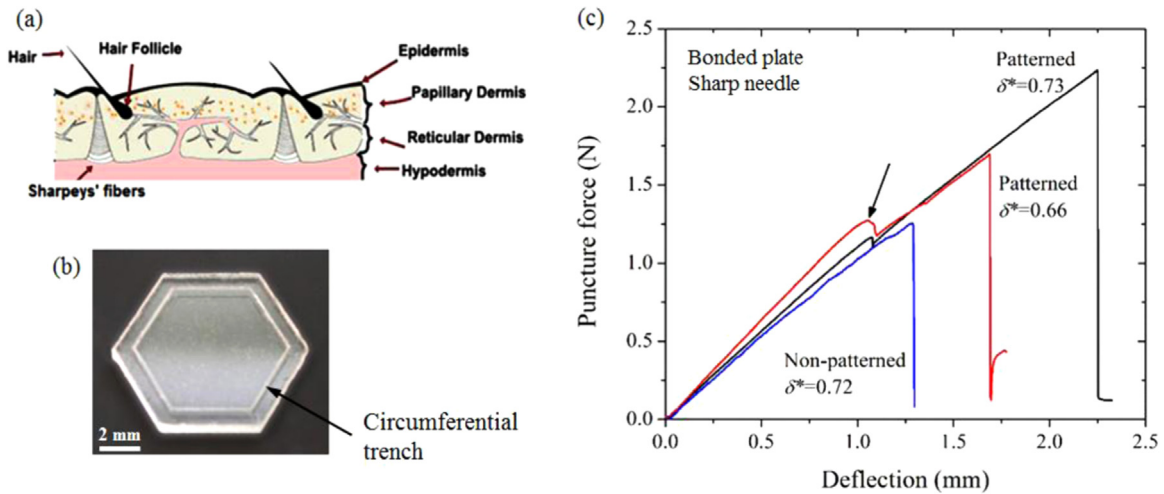
Fig. 15. (a) Schematic of the armadillo osteoderm (adapted from Chen et al., 2011). (b) Picture of a glass hexagonal plate with an engraved circumferential trench. (c) Puncture force–deflection curve for a plate with smooth surface and for a plate with a circumferential trench. (For interpretation of the references to color in this figure, the reader is referred to the web version of this article.).

The possible role of these surface features can be duplicated experimentally by engraving a circumferential trench at a certain distance (here at $\delta^*=0.8$) from the center of the plate (Fig. 15(b)). The force–deflection curves (Fig. 15(c)) for patterned plates (red curve and black curve) show a small drop in force as the critical force is attained (indicated with a black arrow in Fig. 15(c)), but instead of immediately reaching the edge of the sample as seen for the non-patterned sample, the needle gets trapped inside the trench. This enables a new stable equilibrium configuration, which requires a further increase of the puncture force to eventually tilt the plate in an unstable fashion. In this specific case, the trenches doubled the critical force compared to completely smooth plates. The shape and position of the trench can be tuned, and multiple trenches can also be fabricated on the surface of the plate to increase the stability of the plates even further.

(iii) The model shows that F_c^* is governed by δ^*, f, and whether the plate is bonded or non-bonded. These parameters can therefore be chosen to maximize F_c^* as discussed above. However recalling that $F_c^*=\frac{1-\nu}{2\pi\mu R^2}F_c$, the actual critical force F_c can be increased by increasing the size of the plate R. Larger plates promote stability, but they also decrease the overall flexural compliance of the protective armor which may impede movements (λ and Barthelat, 2010). Flexural compliance can however be maintained if flexible plates are used (Vernerey and Barthelat, 2010). Larger plates also increase flexural stresses and therefore decrease the strength of the individual plates (Chintapalli et al., 2014).

(iv) Following the same remark as in item (iii), the model also shows that stability of the plates can be increased by increasing the stiffness of the substrate through $\mu/(1-\nu)$. However increasing the stiffness of the substrate also decreases the flexural compliance of the system, which is detrimental. As for the plate size, a trade-off must be found between flexural compliance and plate stability. Plate size and stiffness substrate should be carefully selected for specific combinations of stability, resistance to plate fracture and flexural compliance.

6. Summary and discussion

Combining hard and stiff plates with soft substrates is a very efficient strategy to achieve high surface hardness to protect against puncture or laceration together with flexural compliance to allow for unimpeded motion. This strategy is common in natural armors (Zhu et al., 2012), and of increasing interest for the design of bio-inspired protective systems (Chintapalli et al., 2014; Rudykh et al., 2015). Here we have investigated a failure mode where the plate remains intact, but suddenly tilts under the action of a localized force. This failure mode is dangerous, and cannot be prevented by increasing the strength of the material of which the protective plates are made. In this work, we have performed a series of experiments to capture the onset of instability of individual glass plates resting on a much softer substrate and subjected to puncture forces from a needle. We developed a simple model which captures the friction of the needle on the plate, the pressure distribution of pressure at the plate–substrate contact area, the effect of bonding the plate on the substrate and the partial lift-off of the plate when it is not bonded. The model captures the salient parameters which control plate stability, and agrees well with the experiments. The main outcome of this analysis is a stability diagram which can serve as guideline for the design of bio-inspired armor. The experiments and the models show that the critical force at which tiling occurs is inversely proportional to the offset distance between the point where the force is applied and the center of the plate. In real applications, the

puncture position cannot be controlled, because the position of the mechanical threat is generally governed by statistics. The model could however be extended to capture the stability conditions under multiple simultaneous point forces (i.e. multiple teeth from a predator) or under a line load (i.e. laceration). The guidelines also highlight a set of parameters which can be optimized at the design stage. Bonding or embedding the plate on or within the soft substrate increases stability and is a relatively easy design to implement. Similar approaches include using ligaments to attach neighboring plates, or using interlocking and/or overlapping so the stability of each plate is improved by the directed contact interaction with its neighbors. This strategy is found in numerous examples in natural armor (Yang et al., 2013a, 2013b), and has the advantage of protecting the weakest areas which are at the boundaries between plates. The onset of stability is triggered by the sudden sliding of the needle on the plate, which can be delayed by increasing the coefficient of friction between the needle and the plate. As demonstrated here, higher friction can be achieved by applying a polymeric coating, or by using roughening the surface. A similar effect can also be achieved by specific morphologies on the surface such as grooves, waviness or con-cavities that can trap the tip of the needle to prevent tilting. Some of these morphologies are observed in natural armors (Chen et al., 2011) and could be systematically implemented in bio-inspired flexural armors. The other two key parameters identified here for the stability of the plate are substrate stiffness and the size of the plates. These parameters are more difficult to optimize, because they also influence the flexural strength of the plates (Chintapalli et al., 2014) as well as the flexural compliance of the system (Vernerey and Barthelat, 2010). The models presented here are valid if the plates can be considered rigid compared to the substrate. This assumption is representative of a large number of natural armor (osteo-derms, ganoid scales) and synthetic armors (glass or ceramic plates on elastomeric or textile substrates). The models could be extended to the cases where the plates deform under puncture, as observed in some light-weight natural protective systems (Zhu et al., 2013). Nevertheless, the guidelines presented here could already be integrated in the near future into more comprehensive design guidelines taking into account stability, compliance and strength. In the process of designing and optimizing materials and architectures for compliant protection, natural dermal armors may still serve as reference and models because their efficacy and versatility is validated by millions of years of evolution.

Acknowledgments

References

Ashby, M.F., 2005. Material Selection in Mechanical Design. Butterwoth-Heinemann.
Barber, J.R., 1984. Some polynomial solutions for the non-axisymmetric Boussinesq problem. J. Elast. 14 (2), 217–221.
Blau, P.J., 2001. The significance and use of the friction coefficient. Tribol. Int. 34, 585–591.
Browning, A., Ortiz, C., Boyce, M., 2013. Mechanics of composite elasmoid fish scale assemblies and their bioinspired analogues. J. Mech. Behav. Biomed. Mater. 19, 75–86.
Bruet, B.J.F., Song, J., Boyce, M.C., Ortiz, C., 2008. Material design principles of ancient fish armour. Nat. Mater. 7 (9), 748–756.
Chen, I.H., Kiang, J.H., Correa, V., Lopez, M.I., Chen, P.Y., McKittrick, J., Meyers, M.A., 2011. Armadillo armor: mechanical testing and micro-structural evaluation. J. Mech. Behav. Biomed. Mater. 4 (5), 713–722.
Chintapalli, R.K., Mirkhalaf, M., Dastjerdi, A.K., Barthelat, F., 2014. Fabrication, testing and modeling of a new flexible armor inspired from natural fish scales and osteoderms. Bioinspir. Biomim. 9 (3), 036005.
Fabrikant, V.I., 1986. Flat punch of arbitrary shape on an elastic half-space. Int. J. Eng. Sci. 24 (11), 1731–1740.
Fabrikant, V.I., 1988. Elastic field around a circular punch. ASME J. Appl. Mech. 55 (3), 604–610.
Funk, N., Vera, M., Szewciw, L.J., Barthelat, F., Stoykovich, M.P., Vernerey, F.J., 2015. Bioinspired fabrication and characterization of a synthetic fish skin for protection on soft materials. ACS Appl. Mater. Interfaces 7, 5972–5983.
Ghosh, R., Ebrahimi, H., Vaziri, A., 2014. Contact kinematics of biomimetic scales. Appl. Phys. Lett. 105, 2337011–2337015.
Hamblin, W.J., 1996. The Roman Army in the First Century. Brigham Young University Studies337–349.
Lawn, B.R., Deng, Y., Miranda, P., Pajares, A., Chai, H., Kim, D.K., 2002. Overview: damage in brittle layer structures from concentrated loads. J. Mater. Res. 17 (12), 3019–3036.
Lin, Y.S., Wei, C.T., Olevsky, E.A., Meyers, M.A., 2011. Mechanical properties and the laminate structure of Arapaima gigas scales. J. Mech. Behav. Biomed. Mater. 4 (7), 1145–1156.
Marino Cugno Garrano, A., La Rosa, G., Zhang, D., Niu, L.N., Tay, F.R., Majd, H., Arola, D., 2012. On the mechanical behavior of scales from *Cyprinus carpio*. J. Mech. Behav. Biomed. Mater. 7, 17–29.
Mirkhalaf, M., Dastjerdi, A.K., Barthelat, F., 2014. Overcoming the brittleness of glass through bio-inspiration and micro-architecture. Nat. Commun. 5, 3166.
Neal, M.L., 2003. Encapsulated Imbricated Armor System. US 6510777 B2.
Robinson, H.R., 2002. Oriental Armour. Dover Edition.
Rudykh, S., Ortiz, C., Boyce, M.C., 2015. Flexibility and protection by design: imbricated hybrid microstructures of bio-inspired armor. Soft Matter 11, 2547–2554.
Sneddon, I.N., 1965. The relation between load and penetration in the axisymmetric Boussinesq problem for a punch of arbitrary profile. Int. J. Eng. Sci. 3 (1), 47–57.
Vernerey, F.J., Barthelat, F., 2010. On the mechanics of fish scale structures. Int. J. Solids Struct. 47 (17), 2268–2275.
Vickaryous, M., Hall, B.K., 2006. Osteoderm morphology and development in the nine-banded armadillo Dasypus novemcinctus (mammalia, xenarthra, cingulata). J. Morphol. 267, 1273–1283.
Yang, W., Chen, I.H., Gludovatz, B., Zimmermann, E.A., Ritchie, R.O., Meyers, M.A., 2013a. Natural flexible dermal armor. Adv. Mater. 25 (1), 31–48.
Yang, W., Gludovatz, B., Zimmermann, E.A., Bale, H.A., Ritchie, R.O., Meyers, M.A., 2013b. Structure and fracture resistance of alligator gar (*Atractosteus spatula*) armored fish scales. Acta Biomater. 9 (4), 5876–5889.
Yang, W., Sherman, V.R., Gludovatz, B., Mackey, M., Zimmermann, E.A., Chang, E.H., Schaible, E., Qin, Z., Buehler, M.J., Ritchie, R.O., Meyers, M.A., 2014.

Protective role of Arapaima gigasfish scales: structure and mechanical behavior. Acta Biomater. 10 (8), 3599–3614.

Zhu, D., Vernerey, F., Barthelat, F., 2011. The mechanical performance of teleost fish scales. Mechanics of Biological Systems and Materials, vol. 2. Springer, New York117–123.

Zhu, D., Ortega, C.F., Motamedi, R., Szewciw, L., Vernerey, F., Barthelat, F., 2012. Structure and mechanical performance of a modern fish scale. Adv. Eng. Mater. 14 (4), B185–B194.

Zhu, D., Szewciw, L., Vernerey, F., Barthelat, F., 2013. Puncture resistance of the scaled skin from striped bass: collective mechanisms and inspiration for new flexible armor designs. J. Mech. Behav. Biomed. Mater. 24, 30–40.